Prompt-gamma track-length estimator with time tagging from proton tracking

Jean Michel Létang, Oreste Allegrini, Etienne Testa

Prompt-gamma track-length estimator with time tagging from proton tracking

Jean M Létang[1], Oreste Allegrini[2], and Étienne Testa[2]

[1] INSA-Lyon, Universite Claude Bernard Lyon 1, CNRS UMR5220, Inserm U1294, Centre Léon Bérard, CREATIS, F-69373 Lyon, France

[2] Universite Claude Bernard Lyon 1, CNRS/IN2P3 UMR5822, IP2I, F-69622 Villeurbanne, France

E-mail: `jean.letang@creatis.insa-lyon.fr`

Keywords: Monte Carlo (MC) simulations, variance reduction techniques (VRT), track length estimator (TLE), prompt gamma (PG)

Abstract. The design of prompt-gamma detectors necessitates numerous Monte Carlo simulations to precisely develop and optimize the detection stages in proton therapy. Alongside the advancement of MC simulations, various variance reduction methods have been explored to speed-up calculations. Among these techniques, track-length estimators are interesting scoring methods for achieving both speed and accuracy in Monte Carlo simulations of rare events. This paper introduces an extension of the GATE vpgTLE module that incorporates the prompt-gamma emission time, which is tagged from the proton tracking, enhancing its utility for studies focused on detector design and optimization that rely on time measurements. The results obtained from a clinical radiotherapy plan are presented. We demonstrate that the new vpgTLE tally with time tagging is accurate, except for certain prompt-gamma lines corresponding to long mean-life nuclei.

Submitted to: *Phys. Med. Biol.*

1. Introduction

Ion therapy has become a recognized method for cancer treatment, but its monitoring is even more decisive than in conventional radiotherapy with X-rays to guarantee a secure dose delivery because of the peaked dose profile. Since no incident particle is likely to exit the patient in the treatment scenario (unlike proton radiography or CT), the monitoring must rely on secondary particles, such as prompt gamma (PG) rays (Krimmer et al. 2018). Numerous Monte Carlo (MC) simulations are therefore required to accurately design and optimize the detection stages or to investigate the PG emission and detection characteristics (Zarifi et al. 2019).

Variance reduction methods have been investigated alongside the development of MC simulations usage (Cramer 1984, Hendricks & Booth 1985). Among MC variance

reduction techniques, track-length estimators are interesting scoring methods to get a fast and accurate MC simulation of rare events, as proposed back in the 80s in the MNCP code (Forster & Godfrey 1985) and formalized for the evaluation of the photon dose with the Kerma approximation (Williamson 1987). In the past few years, several other variations of the TLE have been proposed, such as the neutron-induced gamma dose tally in GATE for radiotherapy applications (Elazhar et al. 2018) and the next-event estimator in Tripoli-4® for neutron transport (Hutinet et al. 2023). The PG source variation of the track-length estimator (vpgTLE) has also been proposed in GATE by (El Kanawati et al. 2015) and a gain of about 1000 in relative uncertainty has been reported for a patient proton therapy treatment plan by (Huisman et al. 2016).

Sophisticated PG detection techniques making use of timing data have recently been proposed, such as PG Spectroscopy (Verburg & Seco 2014, Pausch et al. 2016, Hueso-González et al. 2018, Magalhaes Martins et al. 2020, Wang et al. 2022), PG Timing (Werner et al. 2019, Pennazio et al. 2022), or PG Time Imaging (Jacquet et al. 2021). The design of PG detectors remains quite a challenge however, because it depends on the beam time-structure which itself is accelerator dependent (cyclotrons, synchrotrons, cyclo-synchrotrons...), but the current version of vpgTLE does not record the temporal information in the PG source model. Here, we present an extension of the GATE vpgTLE module (Huisman et al. 2016) that implements the PG emission time making it useful for the detector design and optimization studies that rely on time measurements. Emphasis is just put on the computation of the phantom-specific PG yield distribution, not on the subsequent PG propagation through the geometry (phantom and detectors).

2. Materials and Methods

2.1. PG source model

Without PG time tagging, the PG source model of the vpgTLE code is based on a four-dimensional database, i.e. a volume of PG energy vectors, as described in previous studies (El Kanawati et al. 2015, Huisman et al. 2016). The word "volume" refers in this article to a 3D set where each axis is a direction of space, and the variable indexed by this volume can be a scalar (e.g. HU or dose) or a vector of a non-spatial dimension (e.g. time or energy). A PG energy database has to be built off-line (stage 0 of Figure 1) using analog MC simulations on elemental phantoms. The resulting PG energy distributions are stored in 1D histograms for each proton energy value and then combined into 2D histograms (PG energy as a function of proton energy) for each specific element. Then, during the vpgTLE-tt simulation (stage 1 of Figure 1), the PG energy vector is scored in all voxels along the proton path. It is worth noting that the addition of the PG time tagging to the PG source model would require two contributions: the time-of-flight (TOF) of the proton until the nuclear interaction occurs and the de-excitation time of the target nuclei. While it is possible to store the latter off-line during the database

building, the proton TOF cannot be built in a similar way, and it has to be computed on-the-fly during the MC simulation of the proton tracking. Another concern arises from the way the time dimension is added to the PG source model. The brute-force solution is to add a fifth dimension, but the PG source model would easily reach the terabyte size, making it impractical. Instead of scoring at each voxel a joined 2D PG distribution (i.e. time vs energy), we propose to use the marginal distributions in energy and emission time, and just score the corresponding PG vectors in two separate volumes.

Figure 1 presents the diagram of the vpgTLE method with time tagging (vpgTLE-tt) and the corresponding benchmarking branch with analog MC. Stage 0 is the off-line construction of the database of the PG energy vectors $\boldsymbol{E_{pg}}$ for each proton energy E_p and element of atomic number Z. The scene consists in a set of protons to be tracked in a specific phantom with a given geometry and material composition, provided for example by a treatment plan (RT-plan). In stage 1 of the vpgTLE-tt method, a vector of PG energy ($\boldsymbol{E_{pg}}$) and a double scalar coding the proton time-of-flight (t_{pg}) are scored for each proton step in the corresponding voxels. The stored PG time t_{pg} comes from proton tracking in the target materials, the $\boldsymbol{E_{pg}}$ vector is used to score the PG energy with the TLE method. An analog MC simulation is performed to benchmark the results of the vpgTLE-tt model: in this simulation the PG energy E_{pg} and time t_{pg} are scored as two double scalars only when the proton undergoes a nuclear interaction. The output of the two types of simulations (vpgTLE-tt and Analog) are identical: a volume of the PG energy $\boldsymbol{E_{pg}}$ and emission time $\boldsymbol{t_{pg}}$ spectra (i.e. two 1D histograms for each voxel). In addition, 2D histograms (PG energy vs PG emission time $\boldsymbol{E_{pg}} \times \boldsymbol{t_{pg}}$) are also stored in three voxels of interest (red squares in Figure 3-right) in order to estimate the correlation between these quantites at the scale of a voxel.

2.2. Gate actors

The MC code GATE/Geant4 (Sarrut et al. 2022) is used to implement the vpgTLE-tt method. During the off-line stage 0, run to build the PG database, a scoring actor is used to compute the PG energy data $\boldsymbol{E_{pg}}$ for all proton energies E_p and all elements Z of interest. It has to be noted that in the current implementation of vpgTLE-tt the PG emission by secondary neutrons is not included.

During the online computation of stage 1, two 1D histograms are incrementally updated for each voxel: one with the yield distribution of the PG energy, the second one with the distribution of the PG emission time in the voxel. More specifically, the vpgTLE-tt tally scores one vector (PG energy distribution) and one scalar value (PG emission time) for each proton step all along the proton track. A single proton might score more than once in a given voxel if several proton steps occur in it. During the scoring process, the proton energy (resp. time) is first randomly (uniform) sampled in the proton energy (resp. time) range along the considered step. Then, the PG energy distribution vector is extracted from the PG energy database of the corresponding voxel material at the sampled proton energy, and is added to the 1D histogram containing

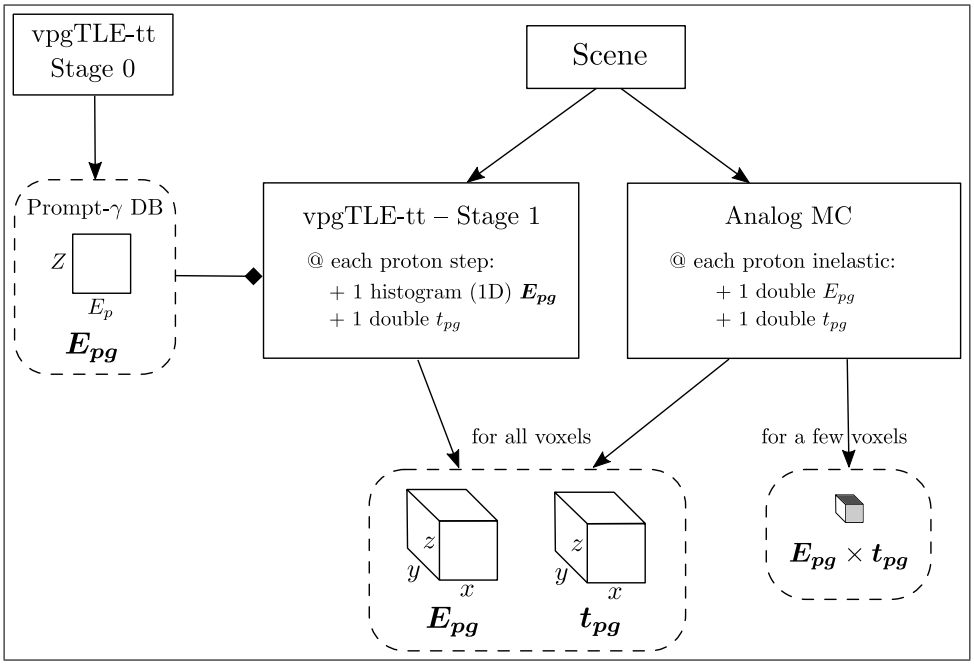

Figure 1. Diagram of the vpgTLE-tt module. Two stages are required to compute the PG emission map with vpgTLE-tt: an off-line stage 0 is run to build the PG database and an on-line stage 1 is run to compute the PG emission maps for the corresponding setup. The analog MC branch is used for benchmarking purposes.

energy distribution vector of the current voxel. The sampled proton time (scalar value) is weighted by the total PG yield of the PG energy distribution vector, and is added to the time distribution vector.

The analog tally scores two scalar values (PG energy and time) only when a proton undergoes a nuclear inelastic process: these scalar values are added to the 1D histograms containing the energy and time distribution vectors for the voxel where the PG emission occurs. In addition, joint distributions of PG energy and time are also scored as 2D histograms for a few voxels of interest.

It is worth noting that the recorded times vary among the actors: the analog actor scores the PG emission time, whereas the vpgTLE-tt actor only scores the proton time. In other words, the nuclear de-excitation time is not taken into consideration in vpgTLE-tt.

2.3. Test cases

The vpgTLE-tt code was tested with simulations on different targets, scenes and phantoms, as described in the following subsections. In all test cases, the Geant4 physics list builder `QGSP_BIC_HP_EMY` has been used with 1 mm production cuts and 1 mm step limiter (Alliso et al. 2016).

2.3.1. PG energy vector database To build the PG energy vector database $\boldsymbol{E_{pg}}$ for each element (from helium to calcium, and titanium, copper, zinc and tin), a statistics

of 10^9 protons of 250 MeV incident to a box of uniform material of density arbitrarily set to unity has been used. The stored PG yield database is normalized in density as described in (El Kanawati et al. 2015), and the scaling by the material density is done at a later time during the initialisation phase of stage 1. Hydrogen is not used since there is no prompt-gamma emission. The following parameters have been set: the proton energy is sampled over 500 bins up to 250 MeV (i.e. 500 keV proton energy samples), the PG energy over 250 bins up to 10 MeV (i.e. 40 keV PG energy samples), and the PG emission time over 250 bins up to 5 ns (i.e. 20 ps PG time samples).

2.3.2. Separability assessment of PG energy and emission time Two setups have been investigated to assess the separability of time and energy informations as it was implemented in vpgTLE-tt: a worst-case scenario and a clinical radiotherapy treatment plan (RT-plan) of a patient. Analog MC simulations have been used to store 2D PG energy and time yields distributions, from which 1D marginal distributions have been computed and compared with the output of the vpgTLE-tt simulation. The product of these two 1D marginal distributions has also been calculated to obtain the 2D distribution equivalent to a model in which PG energy and emission time are not correlated. The 2D distributions of the error difference are computed relatively to the maximum yield count.

The worst-case scenario is shown in Figure 2: a 130 MeV proton beam follows the separation plane of two homogeneous blocks with different stopping powers (bone and lung). The transverse section of the beam is a 1.5 mm radius disk. The proton statistics is 10^8. Each block is $50 \times 500 \times 100\,\mathrm{mm}^3$, and the material compositions are taken from (Valentin 2002). The proton range in the bone block is 72 mm and in the lung block 470 mm. We considered two 2 mm cubic voxels sampled along the proton path at 70 mm from the beam entrance, and located in either side of the separation plane: the one in bone is in thus the Bragg peak, the one in lung in the plateau.

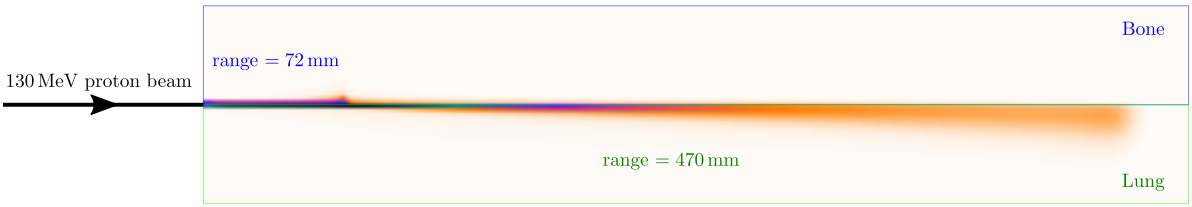

Figure 2. Worst-case scenario: a 130 MeV proton pencil beam impinges upon the interface between two homogeneous blocks (bone and lung).

The clinical case, which consists of the 7 spots of the distal layer of a patient RT-plan, is illustrated with fusion images between the patient CT and the dose map in Figure 3. The corresponding proton energy is 133.08 MeV. Four 2D histograms $\boldsymbol{E_{pg}} \times \boldsymbol{t_{pg}}$ (as described in Figure 1) have been saved with a statistics of 10^9 incident protons: one for the whole volume, and three corresponding to 2 mm cubic voxels along the proton path taken respectively at the entrance, plateau and Bragg peak regions (see transverse

plane of Figure 3).

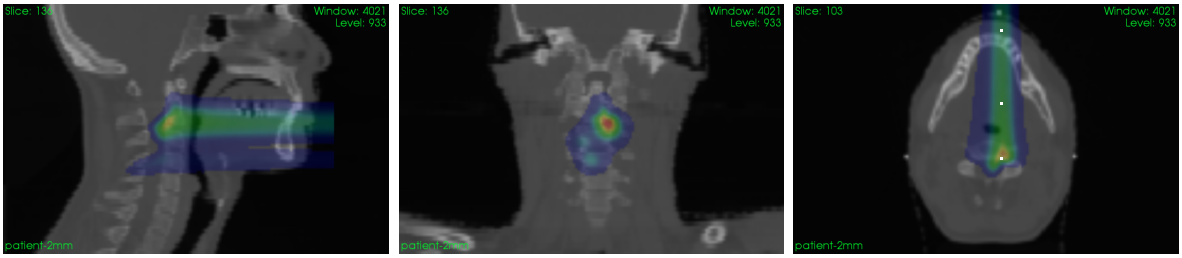

Figure 3. Fusion slices of HU labels and dose distribution of the patient RT-plan used in this study. The small red squares in the transverse plane (right image) show the three voxels of interest, located in the entrance, plateau and Bragg peak regions, respectively.

2.3.3. Impact assessment of nuclear de-excitation time Several excited nuclei produce gamma-ray lines with mean life greater than 10 ps during nuclear de-excitation (Kozlovsky et al. 2002). The delayed gamma-line of oxygen (6.13 MeV and 27 ps mean-life) is a particurlarly interesting case because it is the strongest in the vicinity of the Bragg-peak (Verburg & Seco 2014), i.e. at the end of the proton range where the delayed de-excitation will have much impact on the PG profile. We thus used as phantom a box of $(40 \times 150 \times 40)\,\mathrm{mm}^3$ composed of an oxygen material at unit density to assess the impact of the nuclear de-excitation time. The actors corresponding to the analog and vpgTLE-tt tally have been defined over the whole material box and sampled by 1 mm cubic voxels. The worst case has been selected for this assessment study: the PG energy and emission time are integrated over the whole box. A statistics of 10^7 incident protons of 130 MeV has been used for both actors.

2.3.4. Benchmarking with a patient RT-plan for 3 voxels of interest The benchmarking study is based on the clinical RT-plan described in section 2.3.2 and shown in Figure 3. A statistics of 10^9 incident protons have been used for both the analog and vpgTLE-tt actors, and a scoring volume of $(100 \times 268 \times 100)\,\mathrm{mm}^3$ sampled by 2 mm cubic voxels. Three voxels of interest have been selected to assess the performance of the vpgTLE-tt with respect to the analog MC simulation: in the entrance region, in the plateau region and in the Bragg peak region (depicted as small red squares in the right image of Figure 3).

The efficiency gain $\varepsilon\left(E_{pg}\right)$ for a specific PG energy E_{pg} of the vpgTLE-tt method compared to the analog MC one is defined as:

$$\varepsilon\left(E_{pg}\right) = \frac{T_{\mathrm{analog}}}{T_{\mathrm{vpgTLE-tt}}} \frac{\sigma^2_{\mathrm{analog}}\left(E_{pg}\right)}{\sigma^2_{\mathrm{vpgTLE-tt}}\left(E_{pg}\right)} \tag{1}$$

where T_i and $\sigma_i^2\left(E_{pg}\right)$ are the computation time and variance (of the number of PG of energy E_{pg}) of method i respectively. We used 30 repetitions of both methods to compute an average computation time T_i and the variance $\sigma_i\left(E_{pg}\right)$. This figure-of-merit

is the same as the one that was used in the original PG TLE article (El Kanawati et al. 2015).

3. Results

3.1. PG energy vector database

The PG energy database, shown in Figure 4 for the oxygen element, is the set of PG energy vectors (columns of the image) indexed by proton energy. Recall that the PG database is named as $\mathbf{\Gamma}_Z$ variable in (El Kanawati et al. 2015). It is towards the end of the proton path (for proton energies below a few tens of MeV) that the majority of PG rays are emitted, in particular for oxygen the 4.4 and 6.13 MeV PG lines.

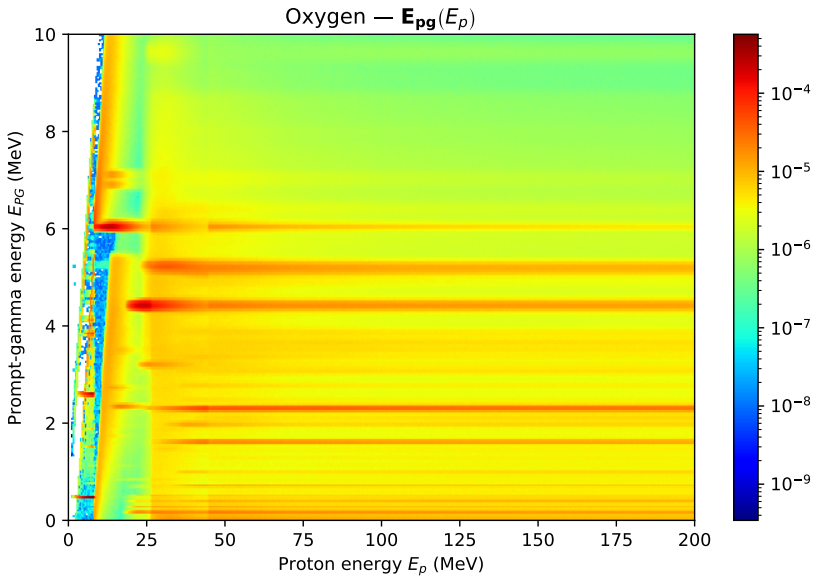

Figure 4. Prompt-gamma elemental database for oxygen. The unit of the look-up table is in number of prompt-gamma per cm and per 40 keV PG energy bin.

The PG elemental database model works well for the vpgTLE-tt tally, it can be computed off-line (e.g. with the use of a computing center) with a large statistics to minimize systematic random errors. There are several points that should be commented however. The proton energy sampling must be fine enough so that the PG energy distribution and the linear material attenuation coefficient related to the proton inelastic nuclear process may be considered piece-wise constant in each proton energy bin, see equation (6) of (El Kanawati et al. 2015). This means however that along a step the proton energy may span several energy bins, and a random energy selection scheme (choice made in this article) must be implemented to avoid a strong step limiter in the MC process or an explicit integration of the PG database inputs. The second point to mention is that the PG database has to be re-built each time the MC physics list changes, but this can be automatized.

3.2. Separability assessment of PG energy and emission time

The assessment of the separability of the gamma energy and time information assumed in vpgTLE-tt was performed by using 2D distributions from an analog MC simulation using the two-block phantom described in section 2.3.2. For each of the two voxels selected respectively in the bone and lung blocks, the joint distributions are shown in Figure 5, together with the 1D marginal distribution based on the separability assumption of vgeTLE-tt model, and the count difference between the two distributions.

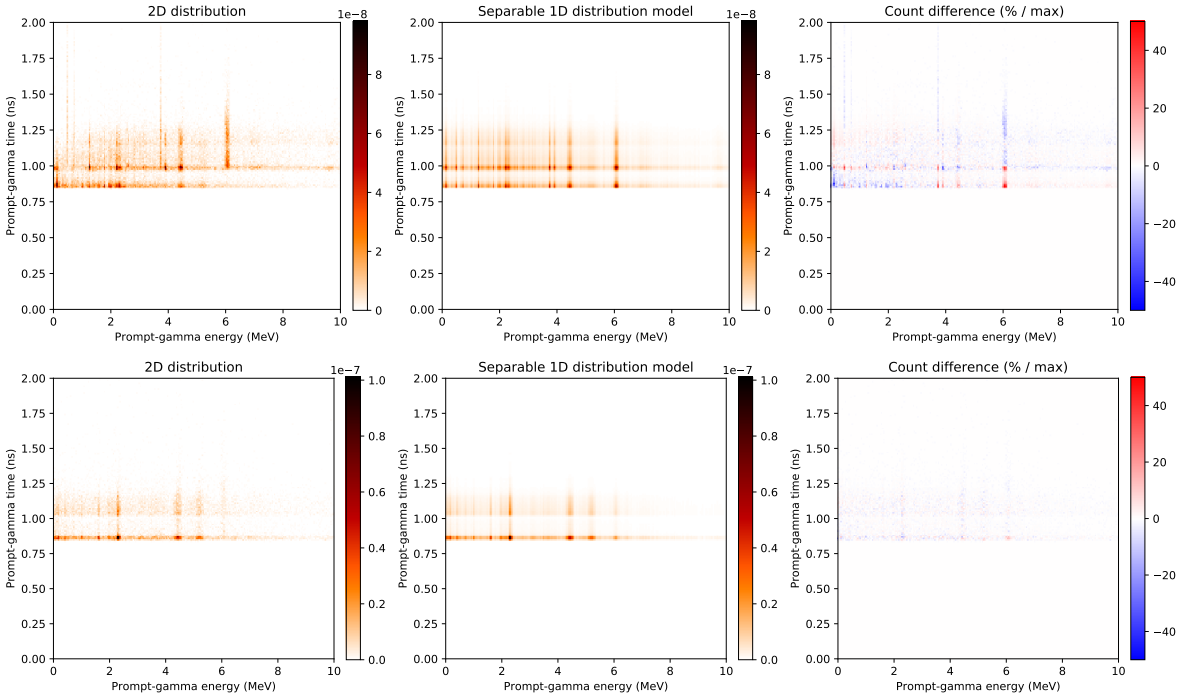

Figure 5. 2D distributions $\boldsymbol{E_{pg}} \times \boldsymbol{t_{pg}}$ (see Figure 1) of PG yields (per proton per 40 keV per 20 ps) for the dual block (see Figure 2) and 10^8 protons of 130 MeV. Top: in the bone $(2\,\mathrm{mm})^3$ voxel. Bottom: in the lung $(2\,\mathrm{mm})^3$ voxel. The voxels are side-by-side, located 70 mm downstream the proton beam (proton range in the bone is 72 mm). The same LUT has been used to keep the color mapping consistent: actual maximum values are respectively 56.6% and 23.8%.

Figure 6 presents the separability tests on the patient RT-plan data. The top row shows the 2D PG time-vs-energy distributions scored for the whole CT volume. The 2D distributions for all three voxels of interest are depicted in row 2 to 4 for the entrance, plateau and Bragg peak regions, respectively. The main PG energy peaks in Figure 6 can be identified as de-excitation energies of calcium, oxygen and carbon (Verburg & Seco 2014). Be aware that the top row of Figure 6 is an extreme case to push the method to its limits, where the whole patient volume is viewed as a single voxel. In practice, the voxelization should be sufficiently fine to get useful results for investigating detector configurations.

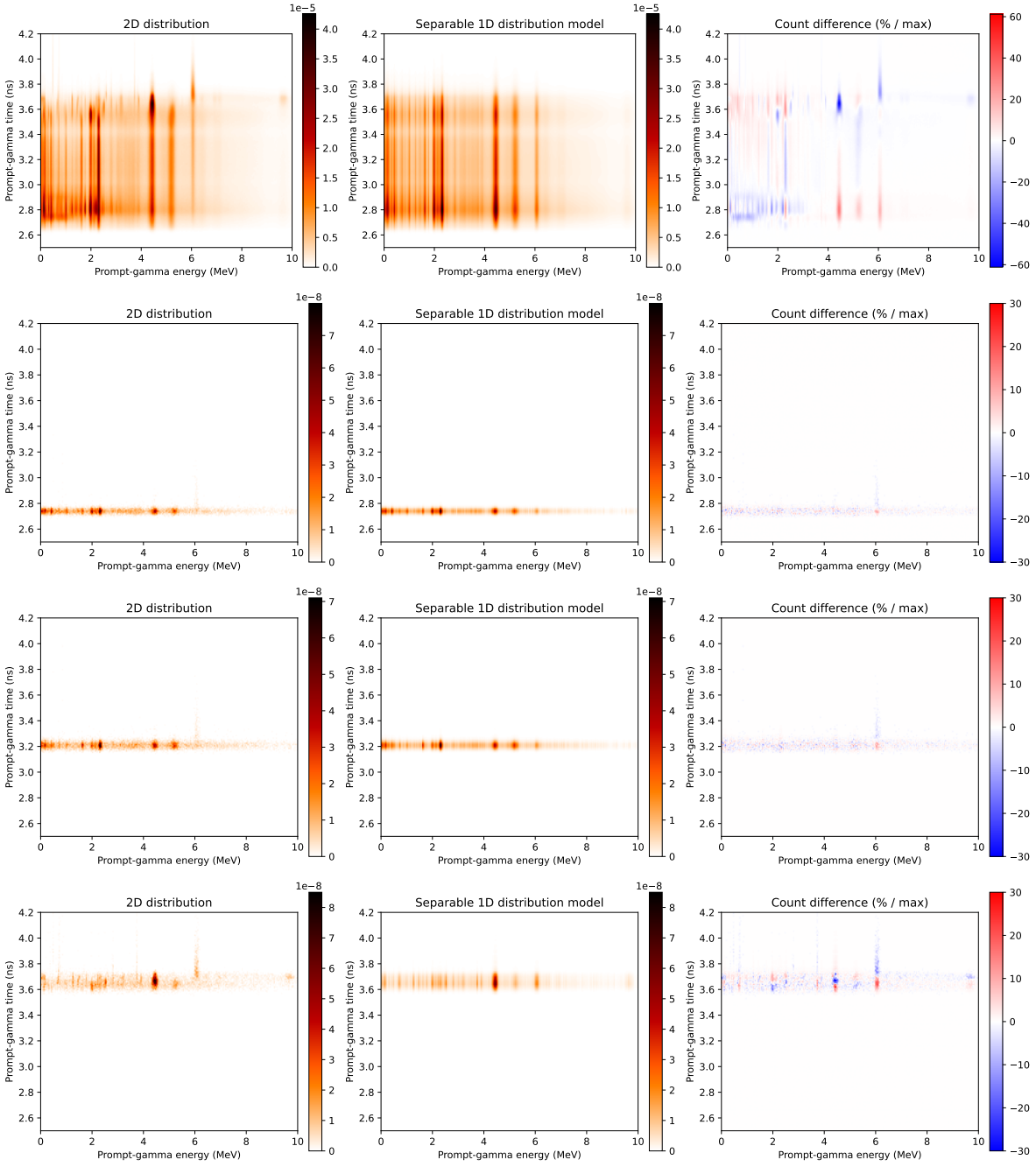

Figure 6. 2D distributions $\boldsymbol{E_{pg}} \times \boldsymbol{t_{pg}}$ (see Figure 1) of PG yields (per proton per 40 keV per 20 ps) for one RT-plan layer (proton energy 130.08 MeV) and 10^9 protons. Top: integrated over the whole patient. Then, from the second row to the bottom row: in the entrance, in the plateau, and in the Bragg peak, all three for a $(2\,\mathrm{mm})^3$ region along the beam path. The same LUT has been used for last three rows of the right column to keep the color mapping consistent: actual maximum values are respectively 17.0%, 18.7% and 38.2%.

3.3. Impact assessment of nuclear de-excitation time

The benchmarking plots (vpgTLE-tt vs analog) corresponding to the PG energy and the PG emission time distributions for the oxygen mono-material test-case are shown in Figure 7. The data is integrated over the whole volume. The error bands correspond to the 99.7% confidence interval of the Poisson distribution of the Analog tally. The confidence interval of the vpgTLE-tt tally is too small and is within the line width.

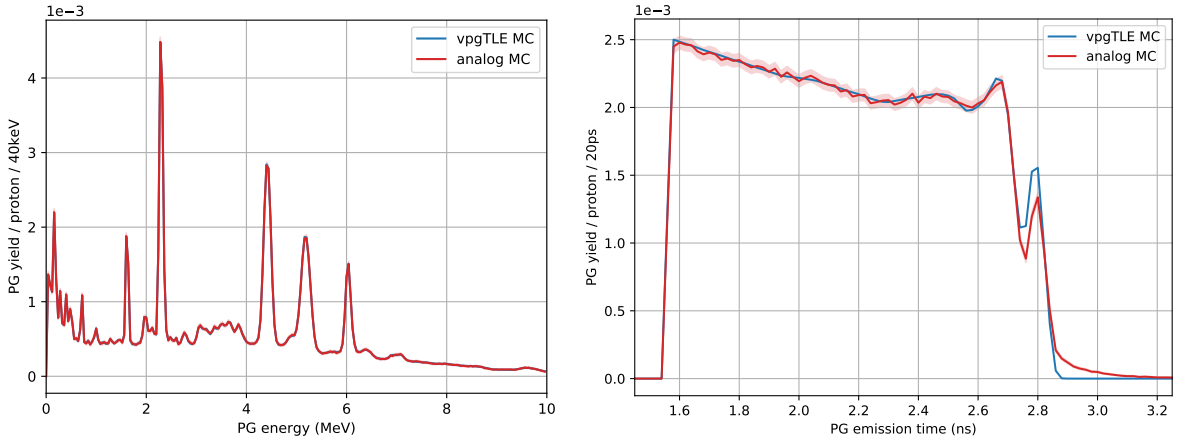

Figure 7. Comparison of the PG energy (left) and emission-time (right) yields between the analog (red) and the vpgTLE-tt (blue) GATE simulations of the oxygen material (density 1). The error band is the 99.7% confidence interval of the Poisson distribution.

3.4. Benchmarking with a patient RT-plan for 3 voxels of interest

The benchmarking plots (vpgTLE-tt vs analog) corresponding to the PG energy (left column) and the PG emission time (right column) distributions for the clinical RT-plan test-case are shown in Figure 8 for all three voxels of interest. The corresponding efficiency-gain plots are shown in Figure 9.

4. Discussion

For the worst-case (bone and lung blocks) scenario depicted in Figure 5, the PG emission-time distributions are given by the superposition of several populations of protons: incident protons with path mainly in the lung block (faster protons), in the bone block (slower protons), and secondary protons (even slower). In the bone voxel (top row of Figure 5), the largest error is for the 6.13 MeV line: PG emitted at about 1 ns are induced by protons at the end of their range (they mainly stayed in the bone block) where this gamma line is the more pronounced, whereas PG emitted at about 0.85 ns are induced by faster protons which traveled mainly in the lung block. In this worst-case scenario, the error of the 1D-separable model is large for the 6.13 MeV line ($> 50\%$), but remains acceptable otherwise ($< 20\%$).

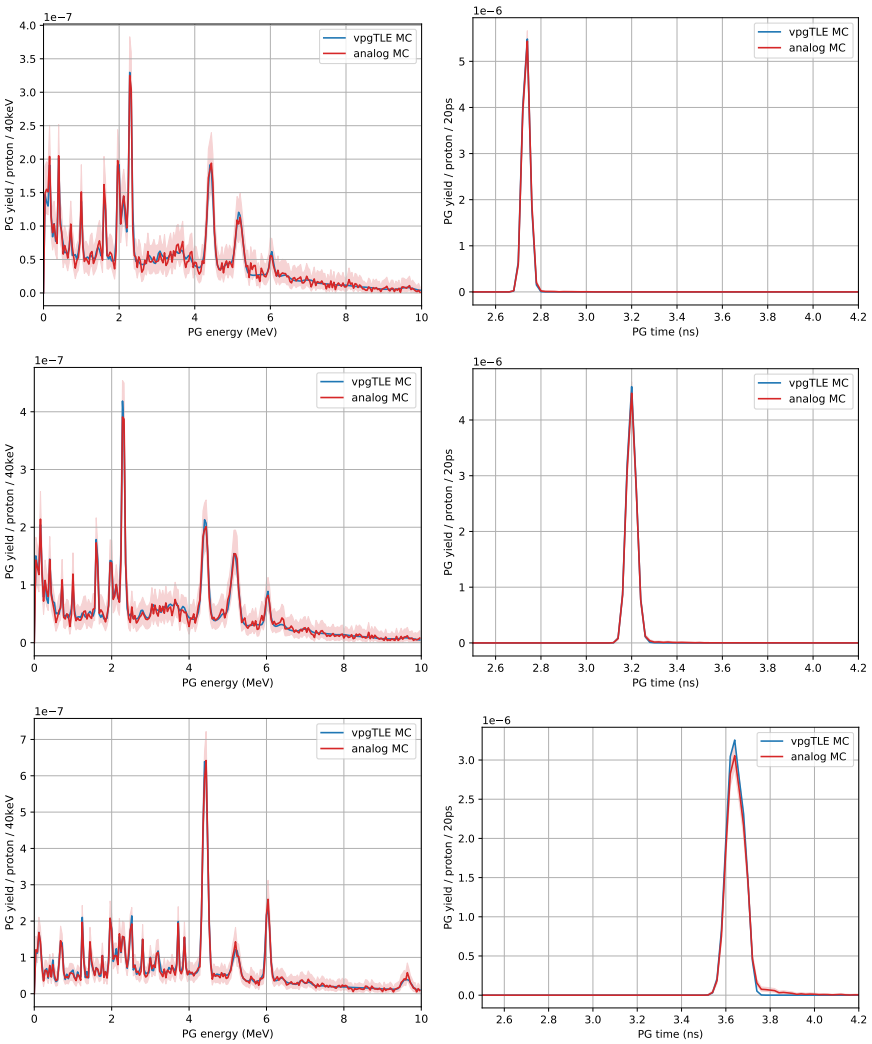

Figure 8. Comparison of the PG energy (left) and emission-time (right) yields for the patient phantom between the analog (red) and the vpgTLE-tt (blue) GATE simulations for three voxels: entrance (top), plateau (middle) and Bragg peak (bottom). The error band is the 99.7% confidence interval of the Poisson distribution.

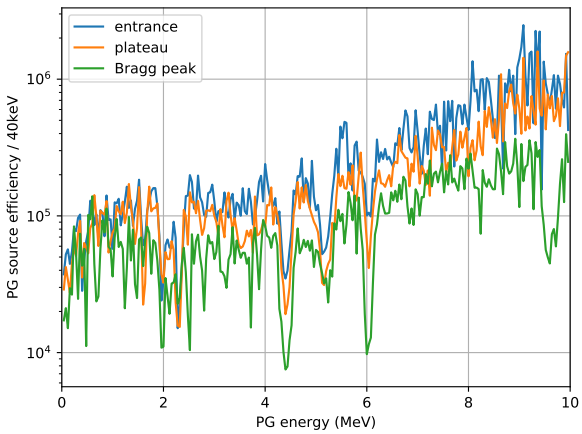

Figure 9. Efficiency curves vpgTLE-tt/analog for the PG source for the three voxels of interest.

The separability assumption – PG emission time vs PG energy – is also not valid on the scale of the whole patient volume, as it can be seen in the first row of Figure 6. Differences larger than 20% occurs because (i) the production of excited nuclei is not uniform all along the proton track, and (ii) the de-excitation time of the target nucleus associated to the PG emission is not always negligible (Kozlovsky et al. 2002). For example, the 6.13 MeV line from excited oxygen nucleus $^{16}O^{*6.13}$ (27 ps mean life) is more likely (i) to be produced in the vicinity of the Bragg peak region (as it can be seen from the PG database of oxygen in the Figure 4) and (ii) to produce a large tail in the time distribution. Other notable gamma lines in the [10 ps, 10 ns] mean-life time range include 0.72 MeV (1 ns), 3.74 MeV (29 ps), and 3.85 MeV (12 ps), but they have a much smaller impact because of their lower cross-sections in PG production. In addition, it is worthy of note that the de-excitation time is below the pico-second for most biologically relevant nuclei as mentioned by (Jacquet et al. 2021). But on a voxel scale (three last rows of Figure 6), the separability approximation is largely valid. This is all the more acceptable given that the best time resolution of the detecting stages is about 100 ps. A solution to overcome this de-excitation time issue in vpgTLE-tt could be to use a specific PG emission time vector for each long mean-life nuclei.

The results on the impact assessment of the nuclear de-excitation time shown in Figure 7 confirms the above conclusions. There is no statistical difference between the vpgTLE-tt tally and the analog MC tally except for the PG emission time at the end of the proton range (i.e. in the PG emission time range of 2.7 to 3 ns according to Figure 7-right), where the production of the 6.13 MeV line is the strongest. But it should be remembered that this study was based on a worst-case scenario, i.e. when the region of interest is the whole volume. At voxel level, agreement is much better, as can be seen for the clinical RT-plan test case in Figure 8: overall no statistical difference for all three voxels of interest between the reference Analog and the vpgTLE-tt simulations but in the time distribution for the Bragg peak voxel. The discrepancy remains rather small however, of the order of 100 ps, i.e. the best time resolution of the detecting stages.

The efficiency gain presented in Figure 9 is between 10^4 to 10^6 depending on the PG energy bin. This is very encouraging. As expected, the smallest efficiency gains correspond to the largest PG lines, such as 4.44 MeV (^{12}C) or 6.13 MeV (^{16}O), because their higher cross sections lead to better statistics than others in the analog MC. If we set the same number of incident protons for both analog and vpgTLE-tt methods, the gain in efficiency only comes from the reduction in variance (the vpgTLE-tt computing time is about 35% longer for the same incident proton statistics).

Once these PG yield distributions (in energy and emission time) are computed for a specific phantom, the next step is to use them as sources of PG emission probability per primary particle (Huisman et al. 2016). Each PG is then propagated through the phantom (and possibly into the detector), according to analog MC protocols.

5. Conclusion

We have presented an extension of the vpgTLE-tt tally with time tagging for Monte Carlo simulations of the prompt-gamma emission sources in proton therapy. It is worth noting that the PG emission-time is just an additional "tag" to the PG energy yield vectors deposited at each step, the timing information does not play any role in the variance reduction. The current vpgTLE-tt implementation is still limited to proton, and PG emission from secondary particles other than protons is not considered yet. As far as proton therapy is concerned, all that remains to be done now is to take into account the PG emission of neutrons by building neutron-specific PG emission databases. The generalization to helium- or carbon-ion therapy is straightforward but tedious since PG emission databases should be built for all particles that induces PG emission, and they are numerous. We have shown that the vpgTLE-tt tally with time tagging is accurate except for some PG lines corresponding to long mean-life nuclei, but the deviations induced by the de-excitation times are less than 100 ps, which is compatible with the temporal resolutions of the detectors currently used for PG detection. A specific handling of such nuclei might be desirable for a better agreement with the analog MC tally.

The vpgTLE-tt method with time tagging is open source and fully integrated in GATE. It will be available in the 2024 release (version 9.4).

Acknowledgments

This work was supported by the LABEX PRIMES (ANR-11-LABX-0063) of Université de Lyon, within the program *Investissements d'Avenir* operated by the French National Research Agency (ANR). We gratefully acknowledge support from the CNRS/IN2P3 Computing Center in Lyon (France) for providing computing and data-processing resources needed for this work. We would like to thank Emma Chetibi and Lorena Laboureau for their help on simulations.

References

Alliso, J., Amako, K., Apostolakis, J., Arce, P., Asai, M., Aso, T., Bagli, E., Bagulya, A., Banerjee, S., Barrand, G., Beck, B. R., Bogdanov, A. G., Brandt, D., Brown, J. M. C., Burkhardt, H., Canal, P., Cano-Ott, D., Chauvie, S., Cho, K., Cirrone, G. A. P., Cooperman, G., Cortés-Giraldo, M. A., Cosmo, G., Cuttone, G., Depaola, G., Desorgher, L., Dong, X., Dotti, A., Elvira, V. D., Folger, G., Francis, Z., Galoyan, A., Garnier, L., Gayer, M., Genser, K. L., Grichine, V. M., Guatelli, S., Guèye, P., Gumplinger, P., Howard, A. S., Hřivnáčová, I., Hwang, S., Incerti, S., Ivanchenko, A., Ivanchenko, V. N., Jones, F. W., Jun, S. Y., Kaitaniemi, P., Karakatsanis, N., Karamitros, M., Kelsey, M., Kimura, A., Koi, T., Kurashige, H., Lechner, A., Lee, S. B., Longo, F., Maire, M., Mancusi, D., Mantero, A., Mendoza, E., Morgan, B., Murakami, K., Nikitina, T., Pandola, L., Paprocki, P., Perl, J., Petrović, I., Pia, M. G., Pokorski, W., Quesada, J. M., Raine, M., Reis, M. A., Ribon, A., Ristić Fira, A., Romano, F., Russo, G., Santin, G., Sasaki, T., Sawkey, D., Shin, J. I., Strakovsky, I. I., Taborda, A., Tanaka, S., Tomé, B., Toshito, T., Tran, H. N., Truscott, P. R., Urban, L., Uzhinsky, V., Verbeke, J. M., Verderi, M., Wendt,

B. L., Wenzel, H., Wright, D. H., Wright, D. M., Yamashita, T., Yarba, J. & Yoshida, H. (2016), 'Recent developments in Geant4', *Nuclear Instruments and Methods in Physics Research Section A: Accelerators, Spectrometers, Detectors and Associated Equipment* **835**, 186–225.

Cramer, S. N. (1984), Variance reduction methods applied to deep-penetration problems, Technical Report 6377987, Oak Ridge National Laboratory.

El Kanawati, W., Létang, J. M., Dauvergne, D., Pinto, M., Sarrut, D., Testa, É. & Freud, N. (2015), 'Monte Carlo simulation of prompt γ-ray emission in proton therapy using a specific track length estimator', *Physics in Medicine and Biology* **60**(20), 8067–8086.

Elazhar, H., Deschler, T., Létang, J. M., Nourreddine, A. & Arbor, N. (2018), 'Neutron track length estimator for GATE Monte Carlo dose calculation in radiotherapy', *Physics in Medicine & Biology* **63**(12), 125018.

Forster, R. A. & Godfrey, T. N. K. (1985), *Monte-Carlo Methods and Applications in Neutronics, Photonics and Statistical Physics*, Springer-Verlag, chapter MCNP - a general Monte Carlo code for neutron and photon transport, pp. 33–55.

Hendricks, J. S. & Booth, T. E. (1985), MCNP variance reduction overview, *in* 'Monte-Carlo Methods and Applications in Neutronics, Photonics and Statistical Physics', Vol. 240, Springer-Verlag, pp. 83–92.

Hueso-González, F., Rabe, M., Ruggieri, T. A., Bortfeld, T. & Verburg, J. M. (2018), 'A full-scale clinical prototype for proton range verification using prompt gamma-ray spectroscopy', *Physics in Medicine & Biology* **63**(18), 185019.

Huisman, B. F. B., Létang, J. M., Testa, É. & Sarrut, D. (2016), 'Accelerated prompt gamma estimation for clinical proton therapy simulations', *Physics in Medicine and Biology* **61**(21), 7725–7743.

Hutinet, H., Le Loirec, C., Mancusi, D., Létang, J. M. & Lyoussi, A. (2023), 'Neutron elastic scattering kernel for Monte Carlo next-event estimators in Tripoli-4®', *The European Physical Journal Plus* **138**(3), 189.

Jacquet, M., Marcatili, S., Gallin-Martel, M.-L., Bouly, J.-L., Boursier, Y., Dauvergne, D., Dupont, M., Gallin-Martel, L., Herault, J., Létang, J. M., Maneval, D., Morel, C., Muraz, J.-F. & Testa, E. (2021), 'A time-of-flight-based reconstruction for real-time prompt-gamma imaging in proton therapy', *Physics in Medicine & Biology* .

Kozlovsky, B., Murphy, R. J. & Ramaty, R. (2002), 'Nuclear deexcitation gamma-ray lines from accelerated particle interactions', *The Astrophysical Journal Supplement Series* **141**, 523–541.

Krimmer, J., Dauvergne, D., Létang, J. M. & Testa, É. (2018), 'Prompt-gamma monitoring in hadrontherapy: A review', *Nuclear Instruments and Methods in Physics Research Section A: Accelerators, Spectrometers, Detectors and Associated Equipment* **878**, 58–73.

Magalhaes Martins, P., Dal Bello, R., Ackermann, B., Brons, S., Hermann, G., Kihm, T. & Seco, J. (2020), 'Pibs: Proton and ion beam spectroscopy for in vivo measurements of oxygen, carbon, and calcium concentrations in the human body', *Scientific Reports* **10**(1).

Pausch, G., Petzoldt, J., Berthel, M., Enghardt, W., Fiedler, F., Golnik, C., Hueso-González, F., Lentering, R., Römer, K., Ruhnau, K., Stein, J., Wolf, A. & Kormoll, T. (2016), 'Scintillator-based high-throughput fast timing spectroscopy for real-time range verification in particle therapy', *IEEE Transactions on Nuclear Science* **63**(2), 664–672.

Pennazio, F., Ferrero, V., D'Onghia, G., Garbolino, S., Fiorina, E., Marti Villarreal, O. A., Mas Milian, F., Monaco, V., Monti, V., Patera, A., Werner, J., Wheadon, R. & Rafecas, M. (2022), 'Proton therapy monitoring: spatiotemporal emission reconstruction with prompt gamma timing and implementation with PET detectors', *Physics in Medicine & Biology* **67**(6), 065005.

Sarrut, D., Arbor, N., Baudier, T., Borys, D., Etxebeste, A., Fuchs, H., Gajewski, J., Grevillot, L., Jan, S., Kagadis, G. C., Kang, G. H., Kirov, A. S., Kochebina, O., Krzemień, W., Lomax, A. J., Papadimitroulas, P., Pommranz, C. M., Roncali, E., Rucinski, A., Winterhalter, C. & Maigne, L. (2022), 'The OpenGATE ecosystem for Monte Carlo simulation in medical physics', *Physics in Medicine & Biology* **67**(18), 184001.

Valentin, J. (2002), 'Basic anatomical and physiological data for use in radiological protection: reference

values', *Annals of the ICRP* **32**(3-4), 1–277.

Verburg, J. M. & Seco, J. (2014), 'Proton range verification through prompt gamma-ray spectroscopy', *Phys Med Biol* **59**(23), 7089–7106.

Wang, J.-L., Wu, X.-G., Li, Z.-F., Xie, S.-Q., Hei, D.-Q., Zhao, Z.-H., Rusanov, A., Zheng, Y., Li, C.-B., Li, T.-X., Zheng, M., Wang, X.-D., Ding, D.-J. & Ruan, H.-S. (2022), 'Prompt gamma spectroscopy retrieval algorithm for element and density measurements accelerated by cloud computing', *Frontiers in Physics* **10**.

Werner, T., Berthold, J., Hueso-González, F., Koegler, T., Petzoldt, J., Roemer, K. E., Richter, C., Rinscheid, A., Straessner, A., Enghardt, W. & Pausch, G. (2019), 'Processing of prompt gamma-ray timing data for proton range measurements at a clinical beam delivery', *Physics in Medicine and Biology* **64**, 105023:1–20.

Williamson, J. F. (1987), 'Monte Carlo evaluation of kerma at a point for photon transport problems', *Medical Physics* **14**(4), 567–576.

Zarifi, M., Guatelli, S., Qi, Y., Bolst, D., Prokopovich, D. & Rosenfeld, A. (2019), 'Characterization of prompt gamma ray emission for in vivo range verification in particle therapy: A simulation study', *Physica Medica* **62**, 20–32.